Energy 239 (2022) 122285

Contents lists available at ScienceDirect

Energy

journal homepage: www.elsevier.com/locate/energy

Theoretical analysis of shape factor on performance of annular thermoelectric generators under different thermal boundary conditions

WenChao Zhu [a, b], Zebin Weng [a], Yang Li [a], Leiqi Zhang [c], Bo Zhao [c], Changjun Xie [a, b, *], Ying Shi [a], Liang Huang [a, **], Yonggao Yan [d]

[a] School of Automation, Wuhan University of Technology, Wuhan, 430070, China
[b] Hubei Key Laboratory of Advanced Technology for Automotive Components, Wuhan University of Technology, Wuhan, 430070, China
[c] State Grid Zhejiang Electric Power Research Institute, Hangzhou, 310014, China
[d] State Key Laboratory of Advanced Technology for Materials Synthesis and Processing, Wuhan University of Technology, Wuhan 430070, China

ARTICLE INFO

Article history:
Received 14 April 2021
Received in revised form
7 September 2021
Accepted 5 October 2021
Available online 11 October 2021

Keywords:
Annular thermoelectric generator
Shape factor
Boundary conditions

ABSTRACT

The annular thermoelectric generator (ATEG) has received growing research interest due to its improved energy conversion efficiency compared to conventional flat-plate thermoelectric generators (FTEG). In this study, considering the influence of ceramic substrate and copper contact layer, a numerical model of the annular thermoelectric module (ATEM) was established for the studies of the influence of geometrical parameters on output performance under three typical application scenarios with different boundary conditions. It is found that when the heat flow on hot side is constant, the shape factors of the optimal performance are slightly different either if the convection coefficient or the temperature is considered constant on cold side. In both cases, the output power and the conversion efficiency decrease with the increase of the thickness of the thermocouple, and increase with the increase of the angle, length, and number of the thermocouples. When the temperatures are considered constant on both sides of the thermocouples, a conflicting relationship between the optimal output power and the efficiency exists. In this case, to obtain the best ATEG performance, multi-optimization problem is formulated and solved by the non-dominant sorting genetic algorithm with elite strategy method (NSGA-II).

1. Introduction

Environmental concerns such as air pollution and depletion of fossil fuels have driven the research of more environmentally friendly energy conversion technologies [1–3]. A thermoelectric generator (TEG) is a device that can convert thermal energy into electricity directly, and it has attracted much research attention in recent years due to its advantages of high reliability and long service life [4–6]. Existing studies have demonstrated the potentials of TEGs in the applications of car exhaust heat recovery [7], solar energy generation [8–10], wireless sensor and monitoring [11], and wearable thermoelectric equipment to recover human body heat [12]. However, subjected to relatively low energy conversion efficiency, there is few real-world applications of the TEG.

In the field of exhaust gas recovery, the TEG is usually attached to the tailpipe of a car to collect the thermal energy absorbed from the hot exhaust fumes. Changing the design parameters of the heat exchanger is an effective means to improve the performance of TEG. Based on the configuration of the heat exchanger as shown in Fig. 1(a), Ref. [13] shows that the net efficiency of TEG can be increased by 5.96% when the optimal inclination angle of the heat exchanger is 2°. Gunay et al. [14] analyzed the intelligent thermoelectric waste gas generator in combination with its economic performance. The power of the thermoelectric module (TEM) in series, composed of 20 HZ-2 material, can reach 41.3 W, and the efficiency is up to 2.15%.

In the field of solar energy generation, Yan et al. [15] studied a new type of flexible thin-film ATEG, and it found that the power that can be generated by a pair of PN legs is 0.14 mW, when the heat flow rate is 2000 W and the cold-side convection coefficient is 5 W/

* Corresponding author. School of Automation, Wuhan University of Technology, Wuhan, 430070, China.
** Corresponding author.
E-mail addresses: jackxie@whut.edu.cn (C. Xie), huangliang@whut.edu.cn (L. Huang).

https://doi.org/10.1016/j.energy.2021.122285
0360-5442/

Nomenclature

symbols

A	cross-section area(m^2)
K_c	constant convective coefficient (W/K)
k	thermal conductivity(W/(m• K))
K	thermal conductance (W/K)
R	electrical resistance (Ω)
r_h	inner radius of thermocouple (mm)
r_c	outer radius of thermocouple (mm)
T	temperature (K)
I	current (A)
H	length of thermocouple (mm)
r	radial direction (m)
m	number of finite element discretization
n	number of thermocouples
P	power (W)
Q	heat flow(W)
Q_{in}	heat absorbed by thermocouple module (W)
Q_{out}	heat released by thermocouple module (W)
Q_{gen}	joule heat generated (W)
V	volume(m^3)
f_1-f_6	calculation constants
T_a	ambient temperature(K)

Abbreviations

FTEG	flat thermoelectric generator
TEM	thermoelectric module
ATEG	annular thermoelectric generator
ATEM	annular thermoelectric module

Greek symbols

α	Seebeck coefficient (V/K)
λ	thermal conductivity (W/(m•K))
σ	electrical conductivity (S/m)
δ	thickness of thermocouple(mm)
$\Delta\varphi$	reference angle(rad)
φ	angle of thermocouple (rad)
η	conversion efficiency (%)
β	angle between thermocouples(rad)

Superscript

i	index of unit $i(i = 1,2,\cdots, m)$

Subscript

cvj	j-th volume element of thermoele-ctric generator($j = 1,2,\cdots,k$)
e	ceramic layer
i	metal contact layer
P	P-type leg
N	N-type leg
L	external load
h	hot side of PN couple
c	cold side of PN couple

K^2. Bellos et al. [16] studied the solar-powered TEGs as shown in Fig. 1(b) from an economic perspective. It was found that when the collection area is 100 m^2, the generated power can reach 5414 kWh, and when the ambient temperature is 293 K and the total radiation solar irradiation is 1000 W/m^2, the efficiency is 3.2%.

In the field of wearable thermoelectric device, the main research areas are concentrated on micro thermoelectric power generation systems and the temperature difference in this area is generally not

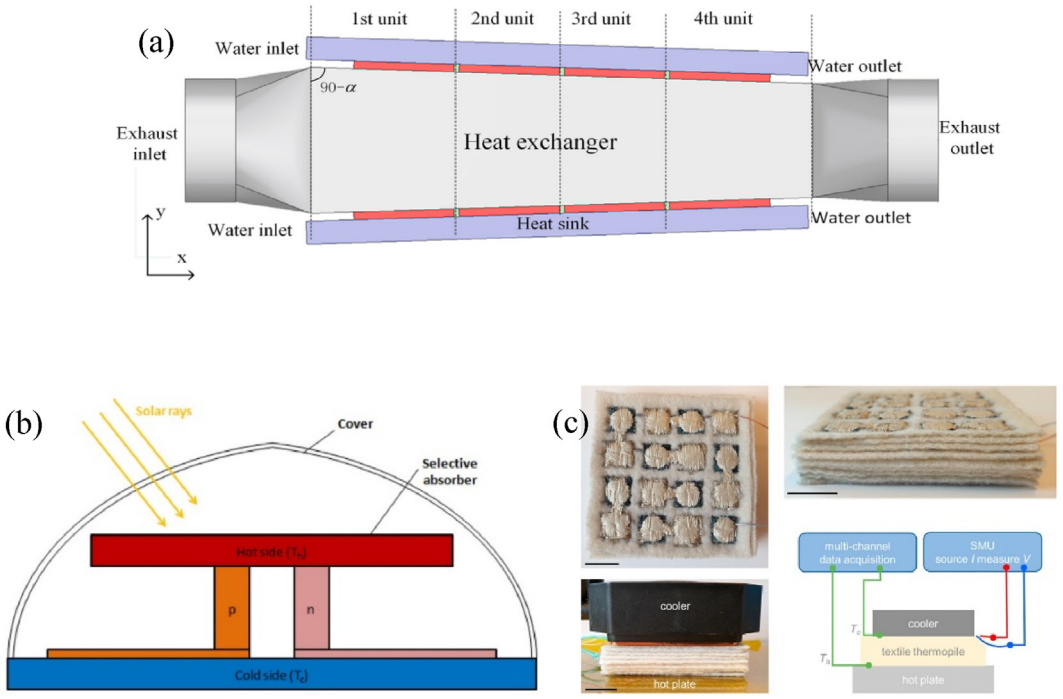

Fig. 1. Structure diagram of TEG in different application fields. (a) schematic of the converging TEG [13]. (b) The solar thermoelectric generator [16]. (c)The embroidered textile thermopile [30].

large. Taking the human body wearable device as an example, due to the constant temperature characteristics of the human skin surface, the boundary condition on the hot and cold sides are generally constant temperature [17]. In Ref. [18], Yuan et al. using FTEG to obtain a boosted output voltage of 2.8−3.3 V through human body temperature, a self-powered wearable multi-sensor bracelet was developed. Anja et al. [19] used electronic textiles to design a new type of micro thermoelectric generator shown in Fig. 1(c). It can be integrated into clothing and 1.2 μW power could be obtained at 65 K. Besides, Hwanjoo et al. [20] and Eric et al. [21] researched on wearable thermoelectric devices and use this as a favorable option for implantable biomedical equipment.

At the same time, the application fields for TEG include Global Positioning Systems (GPS) [22], and the aviation field [17]. Different application fields correspond to different cold and hot side conditions and heat transfer laws, which greatly affect the output performance of TEGs. At the same time, it is very necessary to study the influence of the parameters in the ATEG on the output performance under different scenarios. Optimizing TEG shape factors via numerical study and theoretical analysis are effective methods to obtain improved TEG performance, and the characteristics of the heat source and the materials of the TEG need to be considered in such studies. At present, the optimization of parameters of the TEG is focused on the segmentation or grading of the thermoelectric legs [24,25], the thermoelectric legs with variable cross-sections [26,27], optimization of leg parameters [26,28−31].

A TEG usually consists of a series of TEMs electrically connected in series and thermally connected in parallel, and a TEM consists of N-type legs and P-type legs [18]. The studies on optimization of the leg design are abundant, usually with given materials and the operating environment for a specific application scenario. The optimal selection of the geometrical parameters of the conventional FTEG was investigated in Refs. [19,20] to achieve the maximum output power or the maximum conversion efficiency. Meng et al. [21] suggested that with fixed thermoelectric material volume or TEG bottom area, the maximum output power and the maximum conversion efficiency are closely related to the leg length and the number of thermocouples. The TEM performance of the variable cross-section leg under eight boundary conditions is studied by Liu et al. [22], and the research results show that, under normal circumstances, the variable cross-section leg has a higher conversion efficiency than the cuboid-shaped leg. Sahin et al. [23] find linear cross-sectional area could lead to a reduced output power of TEG. The cross-sectional area could be changed exponentially [24], linearly, or irregularly [25] along the leg length direction. Shu et al. [26] studied the segmented leg-shaped FTEG and applied it to the low temperature difference area of the exhaust pipe to improve the overall heat recovery efficiency. Liang et al. [27] compared the one-stage with two-stage TEGs, and they concluded that with the temperature difference fixed at 40 K, the output power and the conversion efficiency obtained from the two-stage TEG increased by 5.4% and 51.9%, respectively. Fan et al. [28] studied that geometric parameters show various effects on output power and efficiency under different thermal boundary conditions. It showed that the output efficiency is unchanged at the boundary condition of constant temperature and inversely proportional to the cross-sectional area of legs under the boundary condition of constant heat transfer coefficient. Considering the size of legs, He et al. [29] proposed a 1D model of the TEG based on the hill-climbing algorithm. Verified by the 3D numerical model, it was found that for any given leg length, the maximum output power always increased with the increment of leg area.

Although the shape of the leg in TEG has been widely investigated, in most applications the TEG integrated by TEMs is still flat-shaped, which cannot fully fit the cylindrical objects and cause high contact resistance and increased energy loss [31]. In order to address this problem, Shen et al. proposed an annular TEG (ATEG) and analyzed the influence of the leg's geometric characteristics on the output power and efficiency under different temperature ratios and external loads. Thomson effect was considered for the ATEG, and the expressions of the optimal currents for the maximum output power, maximum energy, and maximum exergy efficiency were derived by Kaushik et al. [32], Recently, Shen et al. conducted a comparative study of the ATEG under constant temperature and cross-flow heat sources, and investigated the influence of leg length on the output power of the TEM under different conditions [33]. At the system level, Wang et al. [34] designed a type of ATEG for the natural gas liquefaction process. A comprehensive evaluation method was developed based on the net power output to determine the heat transfer enhancement effect of ATEG [35].

The above-mentioned works on ATEG are valuable, while the results from analysis and simulation are applicable to specific applications based on given boundary conditions. A comprehensive study about the influence of various shape factors on the performance of ATEG is lacking from the literature, while such a study is important to clear the obstacles during the design of the ATEG. In this paper, the boundary conditions of three typical scenarios are studied for parameter research, and the results can provide guideline for the design of the ATEG. In this way, the contributions and innovations of this paper are as follows:

(1) The boundary conditions under three different application scenarios are clarified, and thermoelectric materials with suitable temperature ranges are selected to study different heat transfer laws by MATLAB.
(2) Taking into account the change of material properties with temperature, the finite element method is used to achieve more accuracy. The shape factors that affect the output performance under different boundary conditions has been studied for the first time.
(3) In the case that the maximum output efficiency and power cannot be met at the same time, the NSGA-II algorithm is used to perform multi-objective optimization to determine the shape factors under the optimal output power and efficiency.

This work is structured as follows: A high-fidelity model of the ATEM is established in Section 2. The boundary conditions for three typical applications are analyzed in Section 3. The effect of shape factor on system performance is evaluated in terms of the power and conversion efficiency in Section 4. For the application scenarios with coupling relationship, the multi-objective optimization method is used to find the optimal parameters of the power and conversion efficiency.

2. Modeling of ATEG

Fig. 2(a) presents the 3D structure of a typical ATEG. The ATEG consists of a number of ATEMs and the cross-sectional view of an ATEM is shown in Fig. 2(b). The inner and the outer parts of the ATEG are the hot and the cold sides, respectively, and the outer surface of the ATEG is generally water-cooled or air-cooled. In Fig. 2, '1' and '2' indicate the thermoelement couples made of P-type and N-type semiconductor thermoelectric materials, respectively. Each of the semiconductor components is sandwiched between the heat exchanger and the cold switch. The temperature difference between hot-side and the cold-side junctions causes the directional movement of semiconductor ions which induces a voltage difference. A close loop circuit is achieved by connecting the ATEM with an external load.

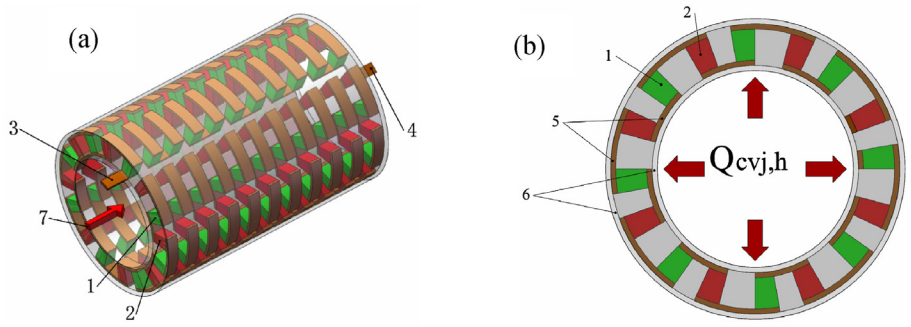

Fig. 2. Structure diagram of ATEG. (a) Main view; (b) Cross-sectional view. 1: P-type leg. 2: N-type leg. 3/4: Positive and negative electrode. 5: Hot/cold contacts. 6: Hot/cold side plate. 7: Heat flow.

The geometrical dimensions of the ATEM are shown in Fig. 3(a) and (b), where β is the angle between the two thermocouples, and θ is the angle between the two legs of the thermocouple. The energy transfer process in the ATEM is shown in Fig. 3(c) with the heat entering the ATEM from the left side. For the i-th module along the pipe, the absorbed thermal energy from the heat exchanger and the thermal energy taken away by the cold exchanger are denoted by $Q_{cvi,1}$ and $Q_{cvi,2}$, respectively.

The following assumptions are made for the development of the ATEG model:

- All the P–N junctions are connected in series with proper insulation.
- Heat only transfers in the radial direction, i.e., the r-axis shown in Fig. 3(b)
- The radiation on all surfaces are ignored.
- All the surfaces except the hot and cold sides are considered as heat insulation.

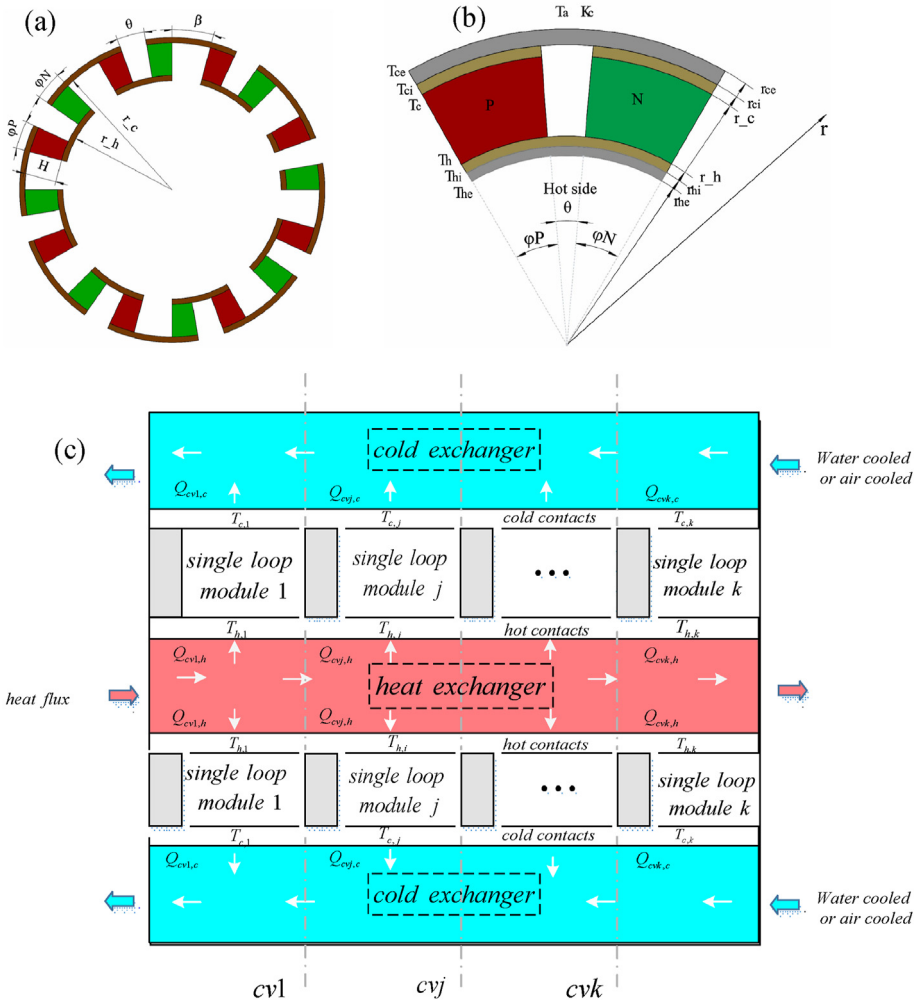

Fig. 3. Schematic diagram of the ATEG. (a) ATEM. (b) Thermocouple. (c) Sectional view.

· Thomson effect is not considered and the thermocouples have symmetrical geometries, which lead to $\varphi_N = \varphi_P = \Delta\varphi, \theta = \beta$, $\delta_P = \delta_N = \delta$, $h_P = h_N = H = r\_c - r\_h$.

One-dimensional steady-state heat conduction process can thus be analyzed for a single ring structure with n pairs of thermocouples. The law of energy conservation yields [36],

$$Q_{in} - Q_{out} + Q_{gen} = 0 \tag{1}$$

where Q_{in}, Q_{out}, and Q_{gen} are the input heat flow rate, the output heat flow rate, and the Joule heat generation rate, respectively.

The heat transfer along the r direction is governed by

$$kA(r)\frac{d^2T}{dr^2} + k\frac{dA(r)}{dr}\frac{dT}{dr} + \frac{I^2}{\sigma A(r)} = 0 \tag{2}$$

where k, σ, T, and I are the thermal conductivity, electrical conductivity, respectively. The cross-sectional area $A(r)$ in (2) can be expressed as

$$A(r) = \Delta\varphi \times r \times \delta \tag{3}$$

Next, the heat flow rate along the r direction can be calculated by

$$Q = -kA(r)\frac{dT}{dr} + \alpha IT \tag{4}$$

The first term on the RHS represents the heat transfer rate based on Fourier's law, and the second term is the Peltier effect, in which α is the Seebeck coefficient. Incorporating the boundary conditions into Eq. (4), the heat flow absorbed by the thermocouple can be obtained as follows. The heat absorbed by the hot side and released by the cold side are

$$Q(r = r\_h) = K\cdot(T_h - T_c) - \frac{1}{2}\cdot I^2\cdot R + \alpha IT_h \tag{5}$$

$$Q(r = r\_c) = K\cdot(T_h - T_c) + \frac{1}{2}\cdot I^2\cdot R + \alpha IT_c \tag{6}$$

$$K = \frac{k\cdot\Delta\varphi\cdot\delta}{\ln r\_c - \ln r\_h} \tag{7}$$

$$R = \frac{\ln r\_c - \ln r\_h}{\sigma\cdot\delta\cdot\Delta\varphi} \tag{8}$$

where K is the thermal conductivity and R is the internal resistance of the thermocouple. Furthermore, $K = K_P + K_N$, $R = R_P + R_N$, and $\alpha = \alpha_P + \alpha_N$, with the subscripts '$P$' and '$N$' denoting the P-type and the N-type legs, respectively.

Fig. 4 presents the resistance network for an ATEM consisting of n pairs of thermocouples. Here, $R_c = R_{hi} + 2R_{ci}$ is the contact resistance, where R_{hi} and R_{ci} are the resistances of the contact layer on the cold and the hot sides, respectively.

For the ATEM, the heat absorbed and released are thus

$$Q_{in} = n\cdot Q(r = r\_h) \tag{9}$$

$$Q_{out} = n\cdot Q(r = r\_c) \tag{10}$$

and n is constrained by

$$n \times (\theta + \Delta\varphi) = \pi \tag{11}$$

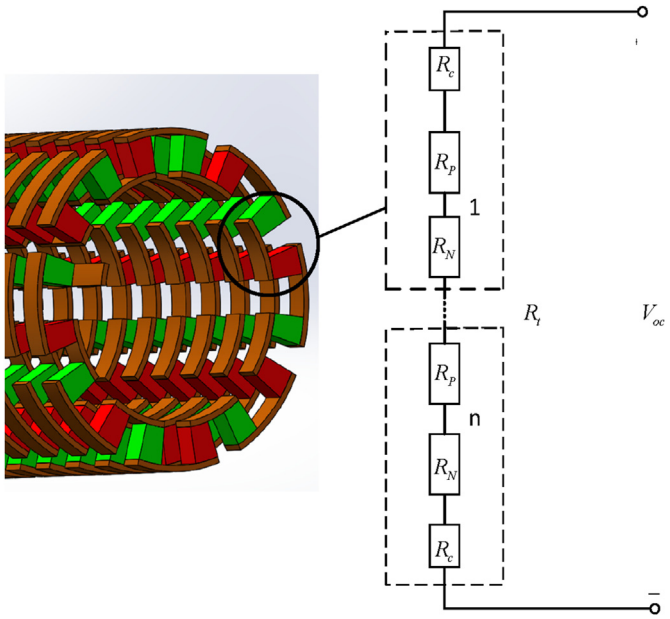

Fig. 4. Resistor network of single ring structure in the ATEM.

$$n < \frac{\pi}{\Delta\varphi_{\min}} \tag{12}$$

Next, the open-circuit voltage and current of the ATEM can be obtained by

$$V_{oc} = n\cdot\alpha\cdot(T_h - T_c) \tag{13}$$

$$I = \frac{V_{oc}}{R_L + R_t} \tag{14}$$

where $R_t = n\cdot(R_N + R_P + R_c)$ is internal resistance of a single ring structure and R_L is the external load resistance.

Finally, when $R_t = R_L$, the output power and the energy conversion efficiency of the ATEM are

$$P_{out} = I^2 \times R_L = \frac{n\alpha^2(T_h - T_c)^2}{4 \times (R_P + R_N + R_c)} \tag{15}$$

$$\eta = \frac{P_{out}}{Q_{cvj,h}} = \frac{n\alpha^2(T_h - T_c)^2}{4 \times (R_N + R_P + R_c)Q_{cvj,h}} \tag{16}$$

Shape factors of this article focuses on the H, σ, δ and θ (or β), because of the constraints of Eqs. (11) and (12), when φ is guaranteed to be certain, we can reflect the influence of θ by studying n, which would reflect the performance of ATEM more intuitively and understandably. So, the research objects of this article focus on H, δ, φ and n. The influence of these shape factors on the output performance of ATEG in different boundary conditions would be discussed later.

3. Analysis of boundary conditions

3.1. Finite element method

Finite element method is used to solve and analyze the model presented in the previous section. As shown in Fig. 5, a pair of thermocouples are discretized into m units [37] and the key parameters of i-th unit are calculated by.

$$\alpha^i = \frac{\int_{T^{i+1}}^{T^i} \alpha dt}{T^i - T^{i+1}}$$
$$k^i = k|_{\frac{T^i+T^{i+1}}{2}} \tag{17}$$
$$\sigma^i = \sigma|_{\frac{T^i+T^{i+1}}{2}}$$

By aggregating the m units, the open-circuit voltage, resistance, and thermal conductance of the thermocouples can be expressed as

$$V_{oc} = n \cdot \sum_{i=1}^{m} \left[\alpha_P^i \left(T_P^i - T_P^{i+1} \right) - \alpha_N^i \left(T_N^i - T_N^{i+1} \right) \right] \tag{18}$$

$$R_N + R_P = \sum_{i=1}^{m} \frac{\ln\left[r^{i+1}/r^i\right]}{\Delta\varphi \cdot \delta} \left(\frac{1}{\sigma_P^i} + \frac{1}{\sigma_N^i} \right) \tag{19}$$

$$K_N + K_P = \sum_{i=1}^{m} \frac{\Delta\varphi \cdot \delta}{\ln\left[r^{i+1}/r^i\right]} \left(k_N^i + k_P^i \right) \tag{20}$$

$$r^i = r\_h + i \cdot (H/m) \tag{21}$$

Eqs. (9) and (10) can thus be expressed as

$$Q_{in} = n \cdot \Big[\times \left(\alpha_P^1 - \alpha_N^1 \right) I T_h + K_N^1 \left(T_h - T_N^2 \right) + K_P^1 \left(T_h - T_P^2 \right) - \frac{1}{2} \cdot I^2 \left(R_N^1 + R_P^1 \right) \Big] \tag{22}$$

$$Q_{out} = n \cdot \Big[\times \left(\alpha_P^m - \alpha_N^m \right) I T_C + K_N^m \left(T_N^m - T_C \right) + K_P^m \left(T_P^m - T_C \right) + \frac{1}{2} \cdot I^2 \left(R_N^m + R_P^m \right) \times \Big] \tag{23}$$

According to the continuity condition at the junctions, we have

$$\alpha_P^i I T_P^{i+1} + K_P^i \left(T_P^i - T_P^{i+1} \right) + \frac{1}{2} I^2 R_P^i = \alpha_P^{i+1} I T_P^{i+1} + K_P^{i+1} \left(T_P^{i+1} - T_P^{i+2} \right) - \frac{1}{2} I^2 R_P^{i+1} \tag{24}$$

The local temperature is governed by

$$T_P^{i+1} = \frac{K_P^i \cdot T_P^i + K_P^{i+1} \cdot T_P^{i+1} + \frac{1}{2} I^2 \cdot \left[R_P^i + R_P^{i+1} \right]}{K_P^i + K_P^{i+1} + \left[\alpha_P^{i+1} - \alpha_P^i \right] \cdot I} \tag{25}$$

Substituting the boundary conditions $T_N^1 = T_P^1 = T_h$ and $T_N^{m+1} = T_P^{m+1} = T_c$ into (25) yields

$$T_h = \frac{Q_{in} \Big/ n + K_N^1 \cdot T_N^2 + K_P^1 \cdot T_P^2 + 0.5 \cdot I^2 \left(R_N^1 + R_P^1 \right)}{\left(\alpha_P^1 - \alpha_N^1 \right) I + K_N^1 + K_P^1} \tag{26}$$

$$T_C = \frac{Q_{out} \Big/ n + K_N^m \cdot T_N^m + K_P^m \cdot T_P^m + 0.5 \cdot I^2 \left(R_N^m + R_P^m \right)}{\left(\alpha_N^m - \alpha_P^m \right) I + K_N^m + K_P^m} \tag{27}$$

Due to the highly nonlinear and coupling relationship between the current I and the temperature distribution, Eqs. (25)-(27) cannot be solved analytically. A numerical method is thus developed by MATLAB to iteratively solve the equations to obtain the output performance, and the flow chart is shown in Fig. 6. By setting the initial temperature, Eqs. (25)-(27) are iterated and substituted into the initial boundary conditions to obtain the final convergence value, and then the current and power conditions after convergence are obtained. Using finite element iteration, the factors are studied under different boundary conditions and the solution.

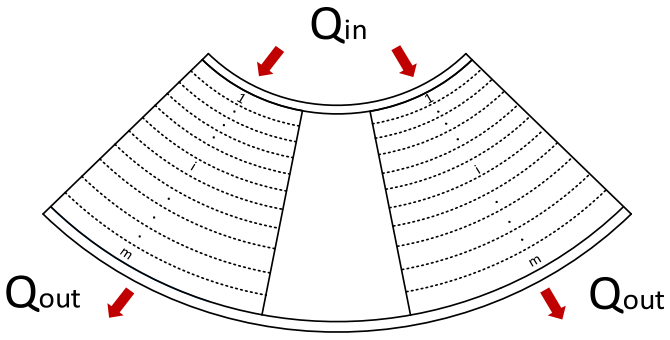

Fig. 5. Finite element analysis of the thermocouple.

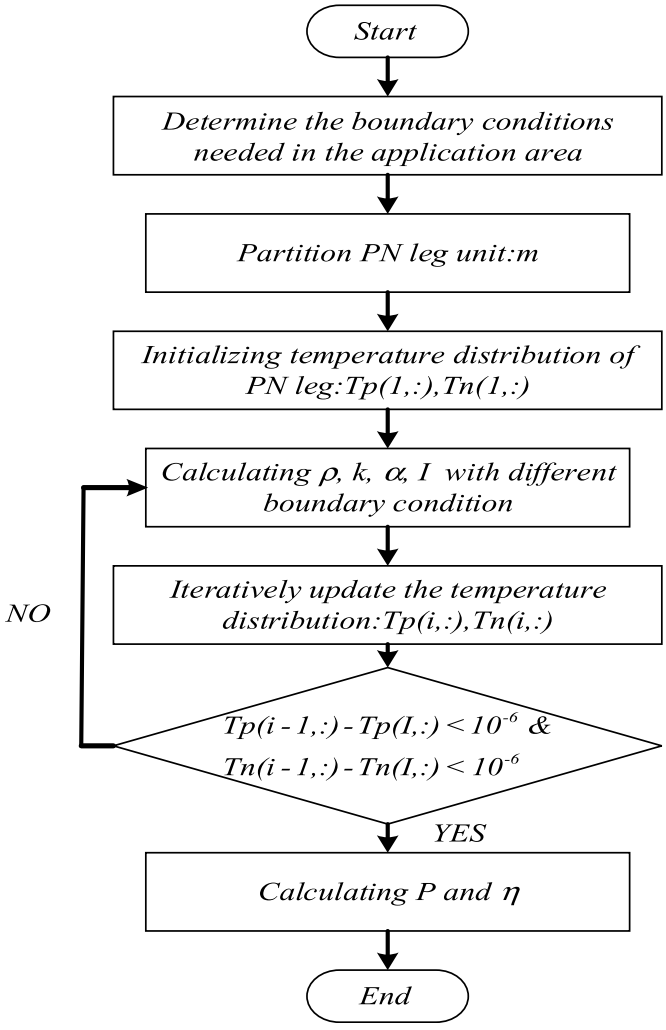

Fig. 6. Model calculation flow chart.

3.2. Application field of ATEG

In this subsection, the ATEG model established in Section 2 is used to study the influence of shape factors on the power and efficiency of the single ring structure in different applications. We will show that for different boundary conditions, the shape factors have different effects on the output performance. The boundary conditions can be divided into the constant temperature, constant heat flow, and constant convection boundary conditions, which are applied to both sides of ATEG respectively, and form nine combinations of possible conditions. Only eight of them exist, while the constant heat flux boundary condition is simultaneously applied to the hot and cold ends, heat conduction equations have no solution [38]. The selection criteria of the boundary conditions in this paper is based on the actual situation, hoping to make explorations for industrial development and practical scientific research to a certain extent. Three of the most common boundary conditions are shown in Table 1 and will be analyzed next, and they correspond to the applications for energy recovery from automobile exhaust gas, biological heat, and solar thermal energy, respectively.

Thermoelectric materials are selected based on the operating temperatures, which can vary significantly for different applications. For example, in the application of vehicle exhaust gas recovery, the temperature is above 700 K [39], the dimensionless figure of merit (ZT) of the P-type or the N-type leg is above 0.6 at 550−750 K, and PbSnTe-based PN-leg semiconductor material is selected [37]. In the field of biomedicine, since the operating temperature is much lower and the temperature difference is small, $(Bi_{0.2}Sb_{0.8})_2Te_3$ is used as the P-type material and $Bi_2(Te_{0.97}Se_{0.03})_3$ is used as the N-type material, ZT of the P-type leg and the N-type leg at room temperature are 0.87 and 0.71, respectively [40]. In the field of solar-thermal energy generation, Bi_2Te_3 is employed as the thermoelectric material, and the ZT can reach a higher level in the range of 400−500 K [41].

In order to control the temperature within the acceptable range, Table 2 lists the default parameters of ATEG for different boundary conditions and geometric parameters of the ATEM [42]. Boundary condition B takes human body heat recovery as an example, the hot side temperature set to 310 K, and the cold side temperature set to 290 K or the ambient temperature [43]. The environmental parameters of boundary condition C are set to the solar scene, and the cold side temperature is assumed to be 303 K [44]. In addition, the parameters of the ceramic layer and the copper contact are: $k_e = 30$ W/(m·K),$\delta_e = 2\delta$,$l_e = 2$ mm,$k_i = 350$ W/(m·K),$\sigma_i = 1 \times 10^7$S/m,$l_i = 1$ mm,$\delta_i = \delta$ [45].

1)Condition A: Constant heat flow on hot side and convection on cold side. Under his condition, the heat is absorbed at a constant rate $Q_{cvj,h}$ on the hot side and the convection coefficient on the cold side is assumed constant. On the cold side, the heat flow rate is determined by

$$Q_{cvj,c} = K_c(T_{ce} - T_a) \tag{28}$$

where T_a is ambient temperature, and K_c is cold-side convection coefficient. Substituting (28) into Eqs. (26) and (27) yields

$$T_h = \frac{Q_{cvj,h} \cdot \Delta\varphi \Big/ \pi + I^2 \times R_{hi} + K_N^1 \cdot T_N^2 + K_P^1 \cdot T_P^2 + 0.5 \cdot I^2 \left(R_N^1 + R_P^1\right)}{(\alpha_P^1 - \alpha_N^1)I + K_N^1 + K_P^1} \tag{29}$$

$$Q_{cvj,c} = \frac{f_1 \cdot (T_c - T_a) + f_2}{f_3} \tag{30}$$

where the coefficients f_1,f_2,f_3, K_{ci}, and K_{ce} are provided in Appendix.

Using Eqs. (23), (27), (28) and (30), the relationship between T_c and K_c can be obtained as

$$T_C = \frac{(f_1 \cdot T_a - f_2) \Big/ (f_3 \cdot n) + 2I^2 \cdot R_{2i} + K_N^m \cdot T_N^m + K_P^m \cdot T_P^m + 0.5 \cdot I^2 (R_N^m + R_P^m)}{f_2/(f_3 \cdot n) + (\alpha_N^m - \alpha_P^m)I + K_N^m + K_P^m} \tag{31}$$

2) Condition B: Constant temperature on hot and cold ends

In the application of bio-thermal energy recovery (e.g., wearable thermoelectric devices), since the temperatures on both sides do not change significantly with the heat flow, they can be considered constant [38]. Based on Eqs. (22) and (23), the heat flow equation in the contact layer of the copper conductor can be expressed as:

$$Q(r = r\_h) = Q_{in} = n \cdot \left(K_{hi} \cdot (T_{hi} - T_h) + 0.5I^2 \cdot R_{hi}\right) \tag{32}$$

$$Q(r = r_{hi}) = Q_{cvj,h} = K_{he} \cdot (T_{he} - T_{hi}) \tag{33}$$

With Eqs. ((6), (9), (22), (23), (32) and (33), the relationship between T_h and T_{he}, and the relationship between T_c and T_{ce} can be obtained as

$$T_h = \frac{f_4 \cdot T_{he} + K_P^1 \cdot T_P^2 + K_N^1 \cdot T_N^2 + 0.5I^2 \cdot \left(R_P^1 + R_N^1\right) + f_5 \cdot I^2}{(\alpha_P^1 - \alpha_N^1) \cdot I + K_P^1 + K_N^1 + f_4} \tag{34}$$

$$T_c = \frac{f_6 \cdot T_{ce} + K_P^m \cdot T_P^m + K_N^m \cdot T_M^m + 0.5I^2 \cdot (R_P^m + R_N^m) + f_7 \cdot I^2}{(\alpha_N^m - \alpha_P^m) \cdot I + K_P^m + K_N^m + f_6} \tag{35}$$

where the coefficients f_4, f_5, f_6, and f_7 are given in Appendix.

3) Condition C: Constant heat flow on hot side and constant temperature on cold side

Table 1
Three typical application scenarios.

Boundary condition	The hot side	The cold side	Application field
A	constant heat flow	convection	Automobile exhaust
B	constant temperature	constant temperature	Wearable device
C	constant heat flow	constant temperature	Solar energy

Table 2
Default parameters under different boundary conditions.

Boundary conditions	$Q_{cvj,h}$ (W)	T_{he} (K)	T_{ce} (K)	K_c (W/K)	n	$\delta/\Delta\varphi/H$ (mm)	r_h (mm)
A	75	–	–	0.25	50	2/0.035/5	75
B	–	310	290	–			25
C	40	–	303	–			40

The heat flow flowing through each ATEM and the temperature on the cold side are considered constant under this condition. The temperature of the hold side and the cold side can be calculated as follows

$$T_h = \frac{Q_{cvj,h}\cdot\Delta\varphi\Big/\pi + I^2\times R_{1i} + K_N^1\cdot T_N^2 + K_P^1\cdot T_P^2 + 0.5\cdot I^2\left(R_N^1 + R_P^1\right)}{(\alpha_P^1 - \alpha_N^1)I + K_N^1 + K_P^1} \tag{36}$$

$$T_c = \frac{f_6\cdot T_{ce} + K_P^m\cdot T_P^m + K_N^m\cdot T_N^m + 0.5I^2\cdot\left(R_P^m + R_N^m\right) + f_7\cdot I^2}{\left(\alpha_N^m - \alpha_P^m\right)\cdot I + K_P^m + K_N^m + f_6} \tag{37}$$

3.3. Model validation

Considering the influence of copper and ceramic substrate, the ATEG models with three different boundary conditions are established. The validity of the models could be verified through the

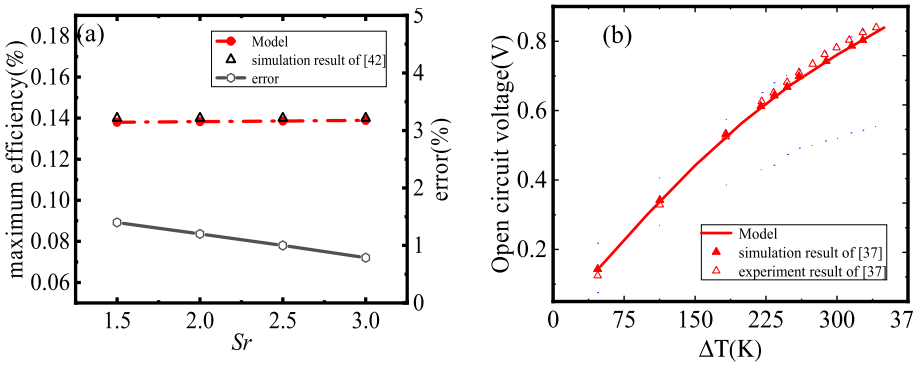

Fig. 7. Model validation.

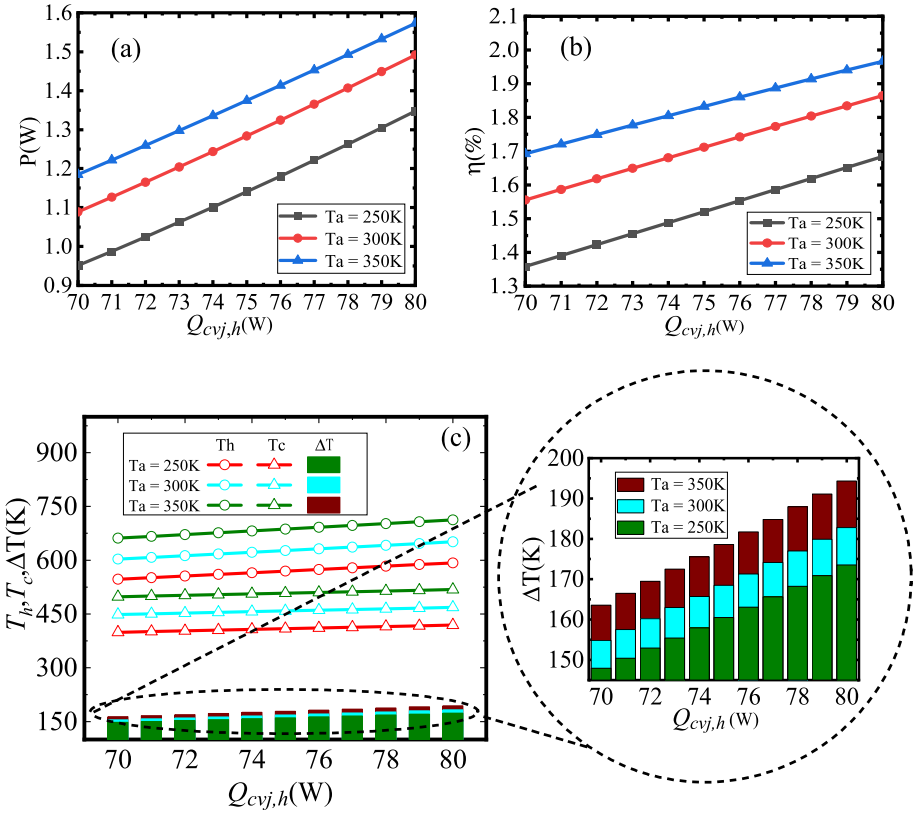

Fig. 8. Effect of heat flow rate on (a) output power, (b) efficiency, (c) temperatures, and temperature difference between the hot and the cold sides.

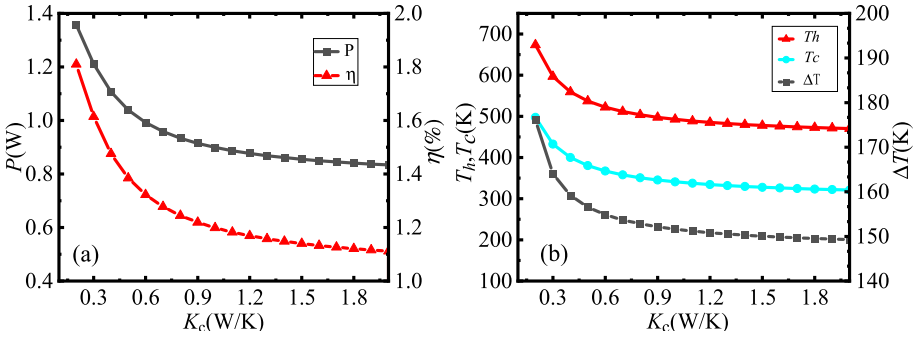

Fig. 9. The effect of convection coefficient on (a) output power and efficiency, (b) temperatures on both sides and temperature difference.

references, but this is only a mechanical repetition and would occupy a large article space. The focus here is to verify the condition B, because the conclusions in this case are relatively complicated. The two conditions A and C would be compared and analyzed in the "Results and discussion" part with the results of other references, which can also be regarded as verifications.

Under the same boundary condition ($T_h/T_c = 2$) and the shape parameters, efficiency calculated by the model are compared with Ref. [46]. As shown in Fig. 7(a), there is a 1.4% difference in the maximum efficiency, reflecting a high degree of consistency under different $Sr = r\_c/r\_h$, which can be explained that the temperature converged by the finite element iteration is different from the given temperature. In this case, the presence of copper strips caused a slight deviation in efficiency, indicating that the model is effective and reliable.

In addition, the model can also be verified by Ref. [40], in which the shape of the thermoelectric leg is rectangular. When r_h is infinite, the thermoelectric leg of the ATEG is similar to rectangular. So, it can be used to verify the simulation results of ATEG. The parameters of flat TEG leg are 1.5 mm in thickness,1.5 mm in length and 10 mm in height respectively, and the cold side temperature is 289 K. The open-circuit voltage is verified by thermoelectric materials used in Ref. [40] and shown in Fig. 7(b). It can be seen that the open-circuit voltage is close the simulation and experimental results in Ref. [34].

4. Results and discussion

4.1. Analysis of boundary condition A

Fig. 8 shows the influence of heat flow rate on the output power, efficiency, temperature, and temperature difference on both sides under the boundary condition A.

When the heat flow rate rises from 70 W to 80 W, Fig. 8(a) and (b) show that by increasing the heat flow rate on the hot side, the output performance of the ATEG can be improved in terms of the output power and efficiency. The output power and efficiency show the same trend, which can be explained by Fig. 8(c). Under this boundary condition, the increase in heat flow rate will lead to temperature rises on both sides of the thermocouple, and result in increased temperature difference, higher output power, and higher efficiency. Similar results are observed in Ref. [37]. In practice, it is also necessary to consider the allowable temperature range of the material used and the ambient temperature. As the heat flow increases, the temperature on both sides of the thermocouple may exceed the temperature suitable for the material.

The influence of the cold-side convection coefficient K_c on the AETG performance is next investigated. As shown in Fig. 9(a) and (b), output power, efficiency, temperatures, and temperature differences all decrease with the increase of K_c. Hence, it is suggested to maintain a low convection coefficient in order to increase ATEG performance. However, to avoid permanent damage to the thermoelectric materials of the ATEG, the maximum temperature must be controlled below the allowable maximum limit, and thus a too small convection coefficient shall not be selected. Therefore, it is necessary to select the thermoelectric material reasonably according to the actual situation to obtain a suitable convection coefficient.

Fig. 10 presents the influence of load ratio R_L/R_t on the output performance of the ATEG. As R_L/R_t increases, both the output power and efficiency increase at the beginning. The maximum power and efficiency are reached at the same time around $R_L/R_t = 1.6$ after which both quantities decrease, which is similar to the optimal value calculated in the literature [47]. The reason why the optimal value does not appear in $R_L/R_t = 1$ is that the change of external load causes the thermal resistance of the PN leg to change. Therefore, there is an optimal thermal resistance matching situation, and the optimal value appears in $R_L = \sqrt{1+ZT_m}R_t$, which is deduced in detail in the literature [48].

Next, we examine the influence of shape factors on the output performance with $n = 50$ and $\Delta\varphi = 1°$, 2°, and 3°. Both the length H and the thickness δ of the leg varies from 1 mm to 5 mm. The effects of the geometrical parameters on the power and efficiency are illustrated in Fig. 11.

Both the power and efficiency slowly increase as the leg length increases, and decrease as the thickness increases. In addition, comparing Fig. 11 (a), (b), (c) at the same time, we can find as the

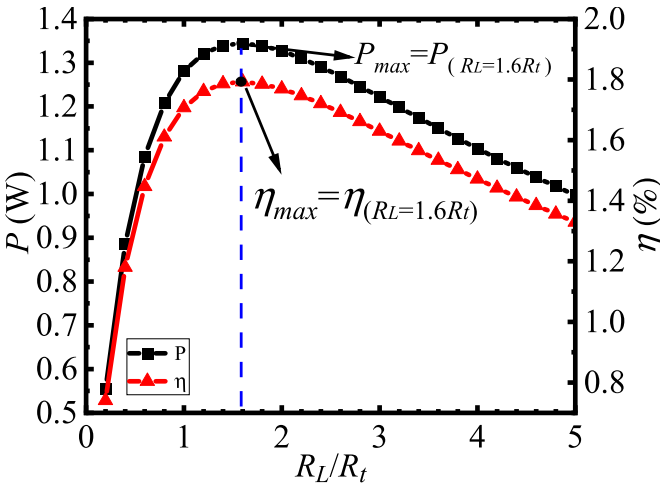

Fig. 10. Effect of load change ratio on output power and efficiency.

angle of the thermocouple $\Delta\varphi$ increases, the power and efficiency increase simultaneously. When $\Delta\varphi = 3°$, excessive leg length exceeds the temperature range of material and the gray part indicates that the power and efficiency are invalid values under corresponding parameters in Fig. 11(c). The maximum power and the maximum efficiency at $\Delta\varphi = 1°$ are about 1.2 W and 1.6%, respectively. When $\Delta\varphi$ increases to 3°, both the maximum power and the maximum efficiency are doubled and they are 2.61 W and 3.48%, respectively. Therefore, it is suggested to increase the leg length or reduce the leg thickness to improve the output performance. However, designs with too thin or too long legs should be avoided since they can reduce the stability and service life of the thermocouples in practical applications.

Fig. (12) shows the relationship between $\Delta\varphi$ and n. To determine the optimal $\Delta\varphi$ and n, the range of $\Delta\varphi$ is set from 1° to 3°, which limits the maximum n to about 180. The changing trend of power and efficiency is shown in Fig. 12. It can be seen that while $\Delta\varphi$ is constant, a large n would benefit the output performance. In other words, the angle θ between the thermocouples should be as small as possible. When n is constant, the output power and efficiency show a consistent trend with the change of $\Delta\varphi$. The larger $\Delta\varphi$ is, the higher the output power and the efficiency can be obtained. So, it is necessary to design the ATEG with a large number of thermocouples and a large $\Delta\varphi$ to obtain a better performance in terms of output power and efficiency.

The reasons for these changes can be analyzed by equations. Substituting Eqs. (13) and (14) into (5), the relationship between the heat flow absorbed by the hot side of each thermocouple and the resistance and thermal conductivity can be obtained as Eq. (38). The left side of (38) is the heat absorbed according to the angle ratio of a thermocouple.

$$\frac{Q_{cvj,h} \times \Delta\varphi}{\pi} = \frac{\alpha^2 T_h}{2(R_P + R_N + R_c)}(T_h - T_c) + K(T_h - T_c) - \frac{\alpha^2}{8(R_P + R_N + R_c)}(T_h - T_c)^2 \tag{38}$$

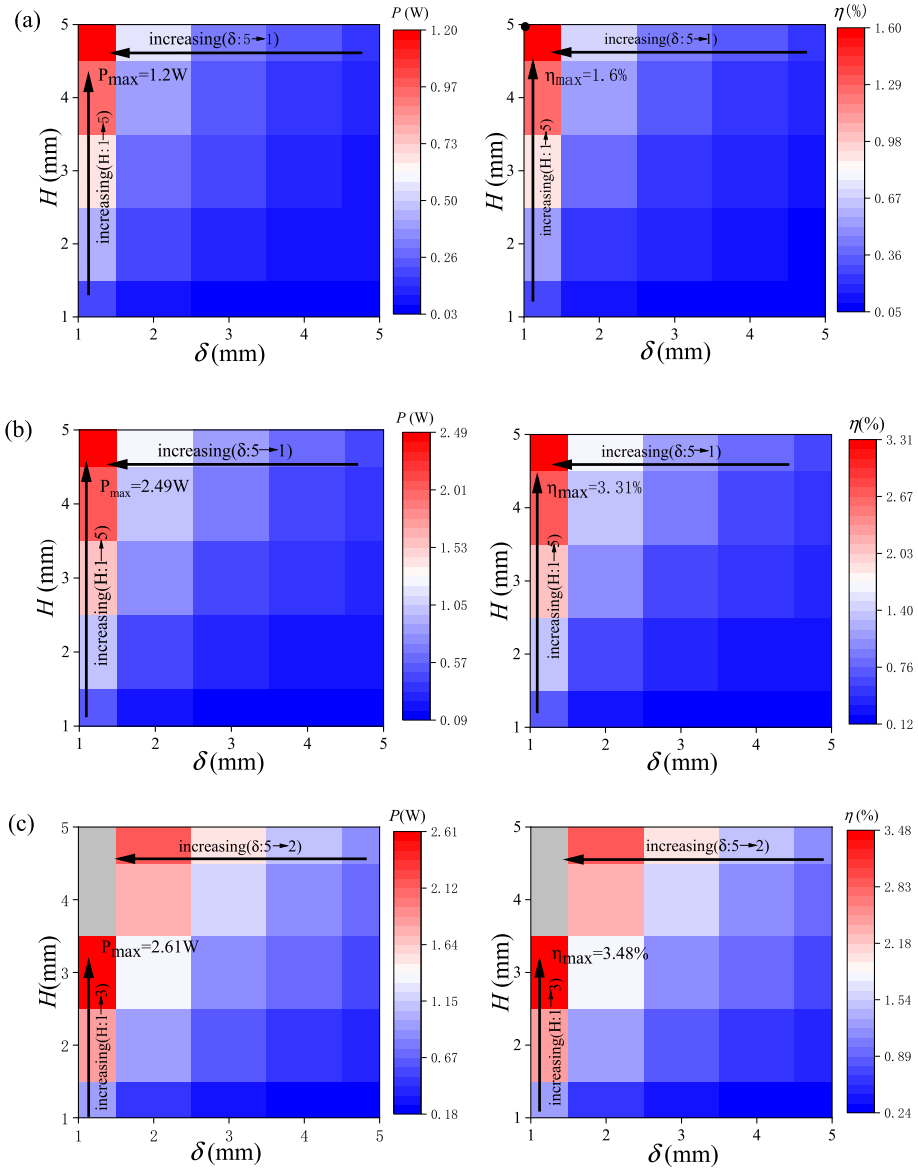

Fig. 11. The influence of geometric parameters on output power and efficiency under the constant heat flow on the hot side and the constant convection coefficient on the cold side with (a) $\Delta\varphi = 1°$. (b) $\Delta\varphi = 2°$. (c) $\Delta\varphi = 3°$.

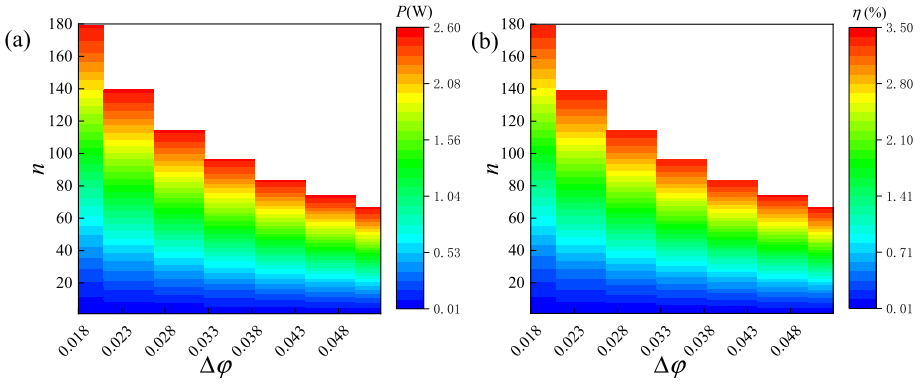

Fig. 12. The influence of n and $\Delta\varphi$ on (a) output power and (b) efficiency.

According to Eqs. (19) and (20), when the leg length H ($H = r\_c - r\_h$) increases, the resistance R_t would increase and the thermal conductivity K would decrease. In this case, $Q_{cvj.h}$ remains constant, in order to maintain a balance, the temperature difference (T_h-T_c) on the right side of Eq. (38) would increase. which means power and efficiency would increase due to the increase in temperature difference. The conclusion is the same of that in Ref. [37].

An increase in thickness would result in a decrease in R_t and an increase in K, which leads to a decrease in temperature difference. It is contrary to the conclusion that increase of leg length, that is power and efficiency would decrease with increase of thickness.

Putting Eqs. (7) and (8) into Eq. (38), the $\Delta\varphi$ could be reduced on both sides of the equation without affecting the temperature difference (T_h - T_c), but the increase of $\Delta\varphi$ would cause the resistance to decrease, which would increase the power and efficiency according to Eqs. (15) and (16).

In addition, increasing the number of thermocouples would also increase the output power and efficiency of the overall single-loop module.

4.2. Analysis of boundary condition B

In this condition, the temperatures on both sides are constant, and the temperature difference is maintained at about 20 K, which can be used to simulate the scenario of bio-thermal energy recovery. Fig. 13 shows how the output power and efficiency vary with the change of the load ratio. In this case, the maximum power is obtained at $R_L/R_t = 1$, while the maximum efficiency is achieved when $R_L/R_t = 1.1$.

The maximum efficiency can be calculated with $R_L = \sqrt{1+ZT_m}R_t$, where ZT presents the dimensionless figure of merit, and the calculated $R_L = 1.1$Rt. Under this boundary condition, since the thermal resistance of ceramic is much smaller than that of PN leg. The temperature difference of the PN leg does not change much under constant temperature conditions, although the external load changes, it does not affect its temperature range. The maximum power point appears near $R_L/R_t = 1$, The maximum efficiency point appears near $R_L = \sqrt{1+ZT_m}R_t$, and the conclusion is the same as that of the literature [46].

When $n = 50$, the output performance for different H and δ is shown in Fig. 14. It can be seen that the efficiency has positive effect with H and not affected by δ, also has little effect with increase of $\Delta\varphi$, while output power increases with increment of δ and decreases with H. For a specific $\Delta\varphi$, the output power decreases with the increase of leg length, but the efficiency increases with the increase of leg length. So, in this application scenario, a reasonable setting of the leg length could significantly improve the performance of the ATEM.

Under the constraint of Eq. (11), the influence of n and $\Delta\varphi$ on the output power and efficiency are shown in Fig. 15. The angle $\Delta\varphi$ varies from 1° to 3°, and n changes from 1 to 180.

As presented in Fig. 15, the maximum power and the maximum efficiency are about 14.75 mW and 1.19%, respectively. It can be seen that a small n leads to high conversion efficiency but low output power. With a specific n, by increasing $\Delta\varphi$, the output power can be increased while the efficiency will drop. Therefore, n needed to be carefully selected to if the requirements on the output power and the efficiency have to be satisfied simultaneously.

Under this boundary condition, the influence of shape factor on power and efficiency may be different from that of boundary condition A. In this case, the temperature at both ends of the ceramic sheet is constant, and the thermal resistance of the copper sheet is very small, and the values of T_h and T_c are almost constant. Incorporating Eq. (8) into Eq. (15), we can get:

$$P_{out} = \frac{n\alpha^2(T_h - T_c)^2}{4 \times \left(\left(\frac{\ln r_c - \ln r_h}{\Delta\varphi \cdot \delta}\right)\left(\frac{1}{\sigma_P} + \frac{1}{\sigma_N}\right) + R_c\right)} \tag{39}$$

The output power P_{out} would decrease with the increase of H ($H = r\_c$-r_h), and increase with the increase of thickness and $\Delta\varphi$

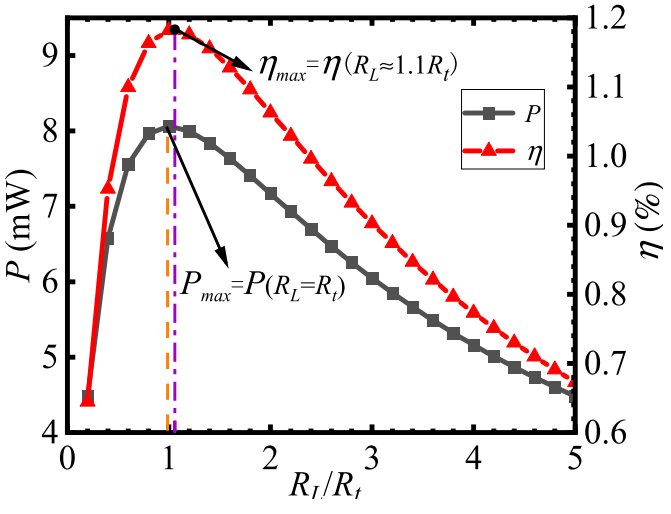

Fig. 13. The effect of load change ratio on output performance.

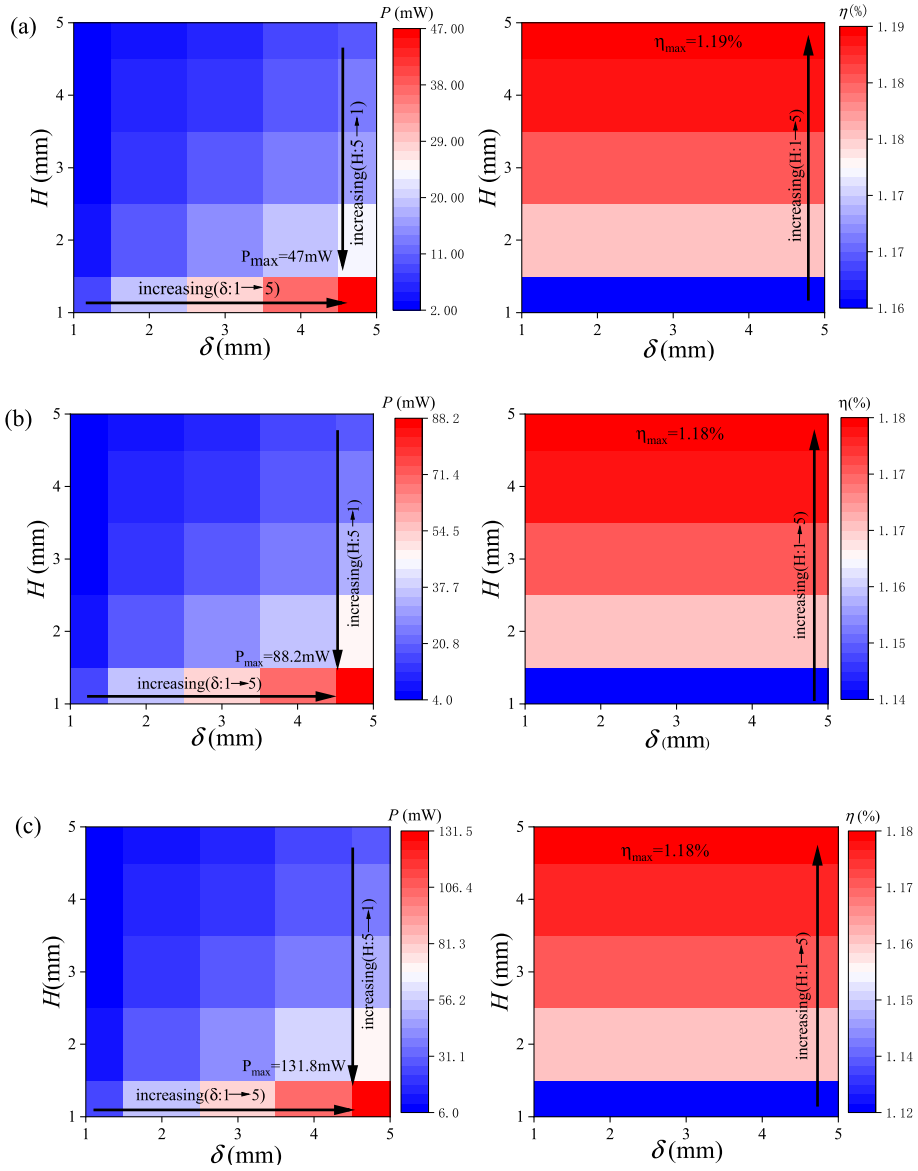

Fig. 14. Effect of geometric parameters on output performance under the boundary conditionB. (a) Output performance at$\Delta\varphi = 1°$(b) Output performance at$\Delta\varphi = 2°$.(c) Output performance at.$\Delta\varphi = 3°$

this is consistent with the MATLAB simulation results.

According to equation (39), ignoring the effect of the copper sheet resistance R_c, the heat absorbed by each pair of PN legs can be expressed by equation (5), so this equation is used to express the conversion efficiency in boundary condition B. Combining equations ((5), (7), (8), (13), (14) and (39), we can get:

$$\eta = \frac{\alpha^2 (T_h - T_c)^2}{2\alpha^2 T_h (T_h - T_c) + 4\sigma k (T_h - T_c) - \frac{\alpha^2 (T_h - T_c)^2}{2}} \tag{40}$$

According to Eq. (40), when temperature difference (T_h–T_c) is constant, the shape factors of thermocouple would not affect the efficiency, which is consistent with the conclusions obtained in most papers and is not consistent with the simulation results of this article. Because thermal resistance of the ceramic chip is considered in this paper, which would make the result more rigorous. The relationship between the temperature difference between the ceramic sheet and the thermocouple can be obtained from the literature [22], and the influence analysis of the shape factors can be completed through this equation, and the influence trend is mutually confirmed with the simulation results of this article.

In summary, when analyzing the power change according to Eq. (39), it is affected by both the temperature difference and the geometric parameter change, and the former is much smaller than the latter, so the slight temperature difference can be ignored. When the efficiency is analyzed according to Eq. (40), it is only affected by the temperature difference, so the change in the temperature difference cannot be ignored by the change of geometric parameters, which leads to the change of the efficiency.

4.3. Analysis of boundary condition C

The condition with constant heat flow on the hot side and constant temperature on the cold side is studied in this subsection, with cold-side temperature being set to 283 K, 303 K, and 323 K, respectively. Fig. 16 shows that both the output power and the

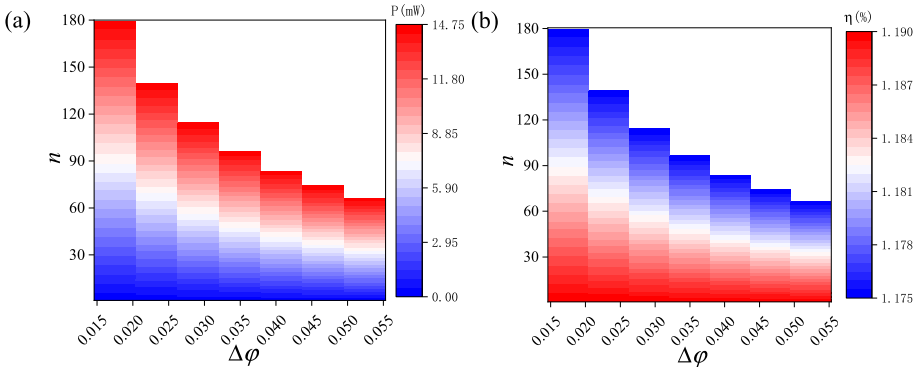

Fig. 15. The effect of changes in$\Delta\varphi$and quantities of thermocouple on output performance. (a)Variation of output power. (b) Variation of efficiency.

efficiency increase with the increase of heat flow rate. At the same time, better output performance can be achieved with a lower the cold side temperature, while is opposite to the trend in Condition A.

Fig. 17 depicts the influence of the load change ratio on the output performance. In this case, the maximum power and efficiency are about 2.1 W and 4.7% respectively. Similar to condition A, both the maximum power and the maximum efficiency are achieved with the same load change ratio, i.e., $R_L/R_t = 1.2$. Under this boundary condition, the constant convection coefficient on the cold side has little effect on the temperature of the PN leg, while the heat flow on the cold side has a greater effect on the temperature, so the situation is similar to the boundary condition A. When the internal and external load relationship satisfies $R_L = \sqrt{1+ZT_m}R_t$, the output power and efficiency reach the maximum at the same time.

When $\Delta\varphi$ is set as 1°, 2° or 3°, the variation of output power and efficiency are studied with the variation of δ and H in Fig. 18. The output power and efficiency change trends are consistent, i.e., they both decrease with the increase of thickness, and increase with the increase of leg length and $\Delta\varphi$.

Fig. 19 shows the variation of output power and efficiency with the consideration of the constraint on $\Delta\varphi$ and n. It can be seen that a larger n or $\Delta\varphi$ can lead to better performance of ATEG. Therefore, for a given heat flow rate on the hot side, the amount of heat absorbed by ATEG has the same positive correlation with n. For a given n, one can improve the performance of the ATEG by increasing $\Delta\varphi$ or reducing θ.

In this case, the condition on the hot side are the same as those in condition boundary A. Although the cold side is different, little

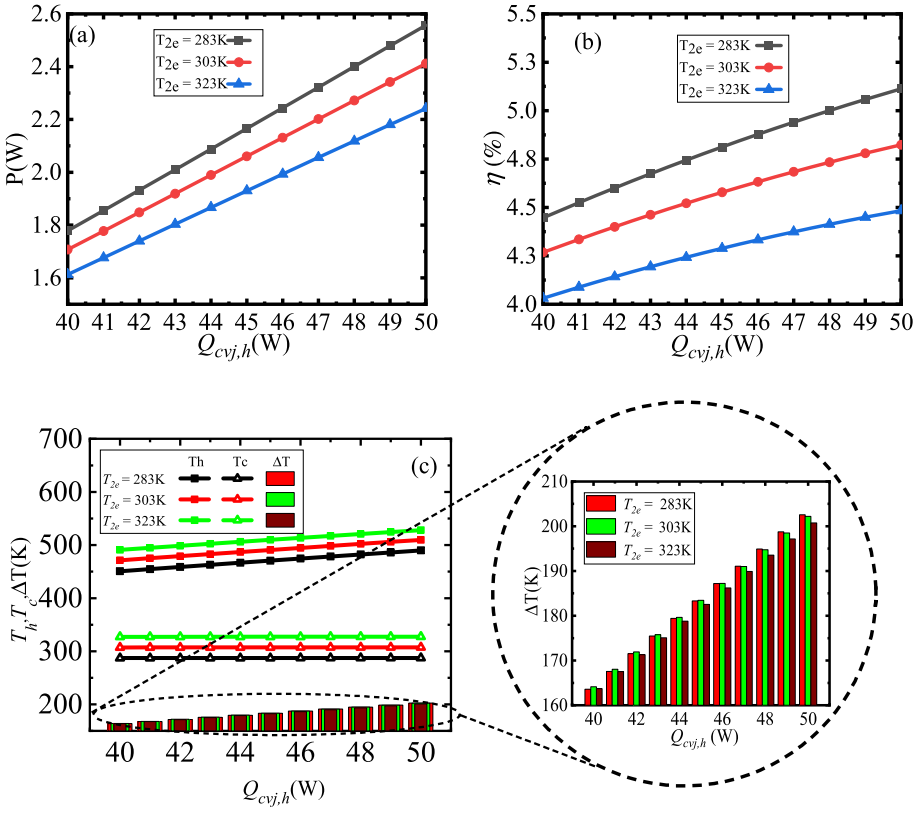

Fig. 16. The effect of heat flow rate on (a) output power, (b) efficiency, and (c) temperatures.

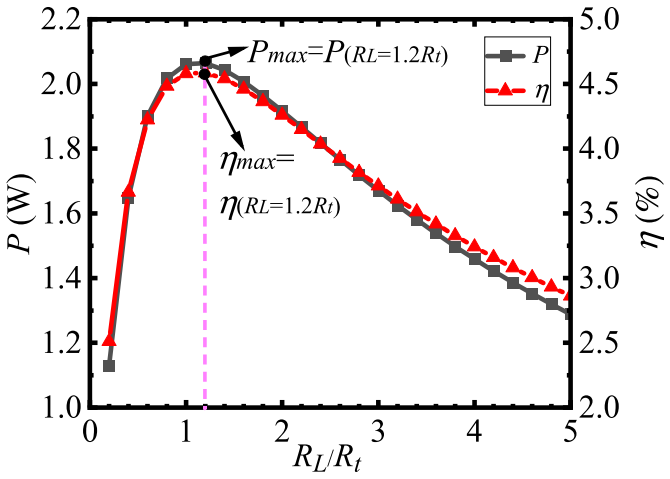

Fig. 17. Effect of load change ratio on output performance.

effect on temperature of thermocouple. We can use the equations of case A to complete the analysis of power and efficiency here.

4.4. Comparison of different conditions

From Section 4.1 to Section 4.3, it can be seen that geometrical parameters may have different influences on the performance of the ATEG under different boundary conditions, and the results are summarized in Table 3. Here, "positive" and "negative" indicate that, by increasing the parametric value, the resulting design performance will be positively or negatively affected, respectively, while "none" indicates that changing the parameter has negligible influence on the performance. An important finding of this study is that the output power and efficiency can be improved simultaneously by turning the shape factors under the boundary conditions A or C. While for condition B, such an optimal design is impossible to achieve since the effects of varying the parameters on the output power and efficiency are opposite and conflicting.

Hence, for condition A or condition C, by increasing the angle,

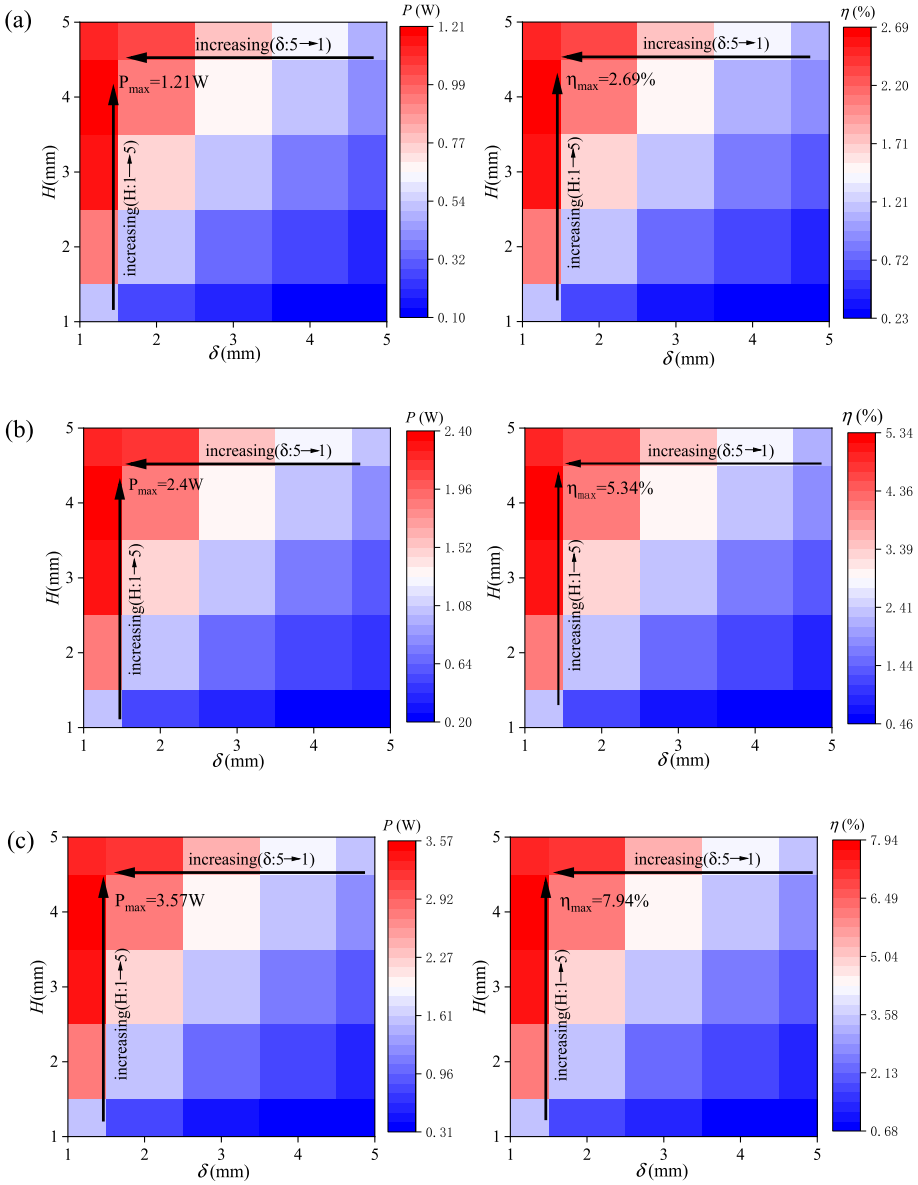

Fig. 18. Effect of geometric parameters on output performance under the boundary condition of constant flow on hot sides and constant temperature on cold side. (a) Output performance at$\Delta\varphi = 1°$.(b) Output performance at$\Delta\varphi = 2°$.(c) Output performance at.$\Delta\varphi = 3°$

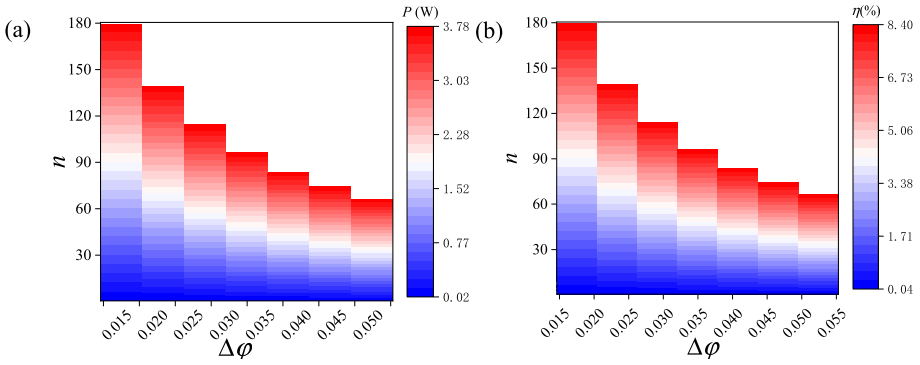

Fig. 19. The effect of changes in $\Delta\varphi$ and n on (a) output power and (b) efficiency.

Table 3
Effect of shape factors on power and efficiency.

Boundary condition	Performance	n	δ	$\Delta\varphi$	H	R
A	P	positive	negative	positive	positive	$R_{\max_{(P)}} = 1.6R_t$
	η	positive	negative	positive	positive	$R_{\max_{(\eta)}} = 1.6R_t$
B	P	positive	positive	positive	negative	$R_{\max_{(P)}} = R_t$
	η	negative	none	negative	positive	$R_{\max_{(\eta)}} = 1.1R_t$
C	P	positive	negative	positive	positive	$R_{\max_{(P)}} = 1.2R_t$
	η	positive	negative	positive	positive	$R_{\max_{(\eta)}} = 1.2R_t$

Table 4
Variation range of NSGA-II algorithm variables.

	$\delta_0 = 1$ mm	$H_0 = 1$ mm	$\Delta\varphi_0 = \pi/180$	$n_0 = 1$
$\frac{\chi}{\chi_0}(\chi_0 = n_0, \delta_0, H_0, \Delta\varphi_0)$	[1,5]	[1,5]	[1,3]	[1,180]

number, and length of the thermocouples and by reducing the leg thickness, theoretical output performance can be improved. However, there are also practical limitations on selecting these parameters, mainly due to the manufacturing technology and stability issues. For example, thermocouples with too thin or too long legs may cause problems with the ATEG structure.

On the other hand, in condition B, since the output power and efficiency cannot be optimized simultaneously, the corresponding design shall be obtained by solving a multi-objective optimization problem.

NSGA-II is one of the methods widely used in the field of multi-objective optimization, and it is thus adopted in this work for the parameter optimization of the ATEM for the boundary condition B. The initial search ranges of the four parameters are set according to Table 4.

NSGA-II is an improved algorithm of NSGA, and its advantages are mainly reflected in the proposal of a fast non-dominated sorting method, which optimizes the algorithm time, and proposes a crowding distance to measure the distribution of the solution and achieve the acquisition of the optimal solution. The basic principle of NSGA-II is shown in Fig. 20. First, the population is initialized, and the initial population is obtained after fast non-dominated sorting, selection, crossover, and mutation operations. Subsequently, the parent population and the offspring population are combined, and then the next-generation population individuals are calculated by sorting and crowding; after the next-generation population is obtained, the next generation is continued to be generated according to genetic operations, and so on, until the set evolutionary generation stop is reached.

By setting the probability of crossover and mutation, the population can generate new individuals and achieve the evolution. The main parameters of NSGA-II are shown in Table 5. The output

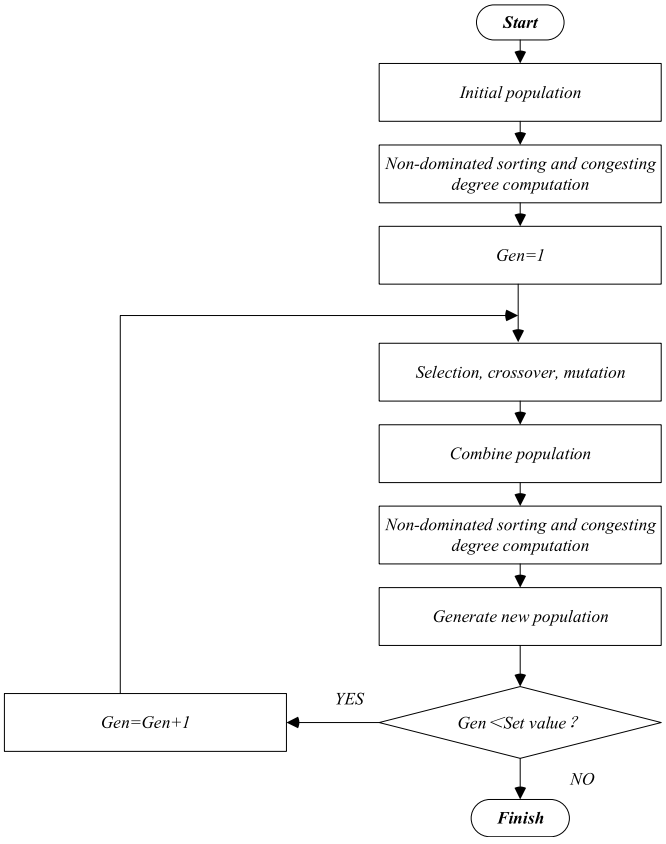

Fig. 20. Flow chart of NSGA-II.

Table 5
The main parameters of NSGA-II.

Parameter	Value/Type
population size	100
genetic algebra Gen	200
crossover probability	0.9
mutation probability	0.1

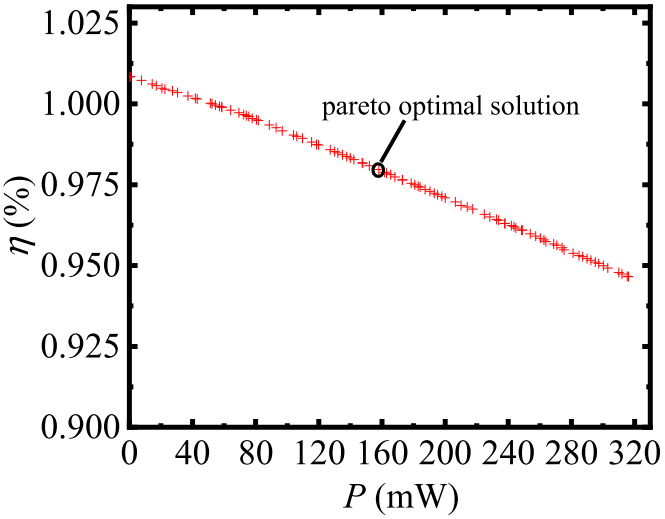

Fig. 21. Optimal results of power and efficiency under boundary condition B.

power and the efficiency of the ATEM under boundary condition B are optimized, and the Pareto optimal solution is obtained through the fast dominance operator and the crowding distance calculation.

Fig. 21 shows the Pareto optimal solution of the output power and the efficiency, the geometric parameters and the obtained output performance are given in Table 6. The efficiency of the thermocouples is related to the temperature difference and the characteristics of the thermoelectric material under different temperature ranges.

5. Conclusion

Based on three typical boundary conditions, different thermoelectric materials are used to simulate the application fields of ATEG and the influence of the structural parameters in ATEM is studied by the finite element method. The study is applicable to the structural design of the ATEG in different scenarios. For a practical application, it is necessary to consider the maximum temperature that the thermoelectric material can withstand to avoid permanent damage caused by excessive heat flow. The main findings of the work are summarized as follows:

(1) In the case of constant heat flow on the hot side and constant convection coefficient or constant temperature on the cold side. Both the output power and efficiency of the ATEM decrease with the increase of the thickness of the thermocouple, and increase with the increase of the angle, length, and number of the thermocouples. At the same time, the performance of ATEM increases with the increase of heat flow on the hot side and temperature on the cold side, but decreases with the increase of the convection coefficient on the cold side. Moreover, the output power and efficiency can reach the maximum when the external load is equal to nearly 1.6 times internal resistance under condition A and 1.2 times internal resistance under condition C.

(2) Under the condition of constant temperature on both sides, the output power increase and conversion efficiency decrease with the increase of the number and the angle of thermocouples. While power decreased and conversion efficiency increase with the increase of leg length. However, the thickness does not affect the conversion efficiency but it has a positive effect on the output power. At the same time, when the external load is equal to the internal resistance, the output power reaches the maximum. And the efficiency reaches the maximum when the load is equal to the internal resistance about 1.1 times.

(3) For conditions B, multi-objective optimization can be used to obtain the optimal design of the thermoelectric devices when it is difficult to obtain the optimal efficiency and optimal power, simultaneously.

Table 6
Optimal parameter values after multi-objective optimization.

boundary condition	n	δ(mm)	$\Delta\varphi$	H (mm)	P (mW)	η (%)
B	100	5	0.03	2.14	158	0.98

Author contributions

WenChao Zhu: Data curation, Funding acquisition, Investigation, Writing – original draft, Zebin Weng: Data curation, Software, Writing – original draft, Yang Li: Formal analysis, Investigation, Writing – review & editing, Leiqi Zhang: Formal analysis, Validation, Bo Zhao: Conceptualization, Project administration, Supervision, Changjun Xie: Conceptualization, Funding acquisition, Project administration, Supervision, Writing – review & editing, Ying Shi: Methodology, Software, Liang Huang: Conceptualization, Validation, Yonggao Yan: Funding acquisition, Methodology.

Declaration of competing interest

The authors declare that they have no known competing financial interests or personal relationships that could have appeared to influence the work reported in this paper.

Acknowledgments

This research was supported by the National Natural Science Foundation of China (51977164), the Wuhan Frontier Project on Applied Research Foundation (2019010701011405) and "the Fundamental Research Funds for the Central Universities" under grant 2021-zy-024.

Appendix

Thermal conductance and electrical resistance of contact layer

$K_{he}$is the thermal conductance of$T_{he}-$ endand$T_{hi}-$ end, which is

$$K_{he}=\frac{k_e\cdot(2\pi)\cdot(2\cdot\delta)}{\ln(r_{hi})-\ln(r_{he})} \tag{A.1}$$

$K_{hi}$and$R_{hi}$are the thermal conductance and electrical resistance of hot contact, which is $T_{hi}-$ endand T_h- end, defined as

$$K_{hi} = \frac{k_i \cdot (2 \cdot \Delta\varphi + \theta) \cdot \delta}{\ln(r_{hi}) - \ln(r_{he})} \tag{A.2}$$

$$R_{hi} = \frac{\ln(r\_h) - \ln(r_{hi})}{\sigma_i \times \delta \times (2 \times \Delta\varphi + \theta)} \tag{A.3}$$

$K_{ci}$and$R_{ci}$are the thermal conductance and electrical resistance of hot contact, which is $T_c -$ endand $T_{ci} -$ end,is

$$K_{ci} = \frac{k_i \cdot \Delta\varphi \cdot \delta}{\ln(r_{ci}) - \ln(r\_c)} \tag{A.4}$$

$$R_{ci} = \frac{\ln(r_{ci}) - \ln(r\_c)}{\sigma_i \times \delta \times \Delta\varphi} \tag{A.5}$$

$K_{ce}$is the thermal conductance of$T_{ci} -$ endand$T_{ce} -$ end, which can be expressed

$$K_{ce} = \frac{k_e \cdot (2\pi) \cdot (2 \cdot \delta)}{\ln(r_{ce}) - \ln(r_{ci})} \tag{A.6}$$

Expressions of some parameters, $f_1, f_2, f_3, f_4, f_5, f_6, f_7$ in Eqs. (36), (39) and (40)

$$f_1 = 2 \cdot n \cdot K_{ci} \cdot (K_c + K_{ce}) \tag{A.7}$$

$$f_2 = n \cdot I^2 \cdot R_{ci} \cdot (K_c + K_{ce}) \tag{A.8}$$

$$f_3 = 2 \cdot n \cdot K_c \cdot K_{ce} \cdot K_{ci} + K_c + K_{ce} \tag{A.9}$$

$$f_4 = n \cdot K_{hi} \cdot R_{hi} + 0.5 K_{he} \cdot R_{hi} \tag{A.10}$$

$$f_5 = K_{he} \cdot K_{hi} / (n \cdot K_{hi} + K_{he}) \tag{A.11}$$

$$f_6 = 2K_{ce} \cdot K_{ci} / (2n \cdot K_{ci} + K_{ce}) \tag{A.12}$$

$$f_7 = R_{ci} \cdot K_{ce} / (2n \cdot K_{ci} + K_{ce}) + 2R_{ci} \tag{A.13}$$

References

[1] Bell LE. Cooling, heating, generating power, and recovering waste heat with thermoelectric systems. Science 2008;321:1457–61.
[2] Champier D. Thermoelectric generators: a review of applications. Energy Convers Manag 2017;140:167–81.
[3] Xiaolong L, Changjun X, Shuhai Q, Liang H, Fang Wei. Energy management strategy of thermoelectric generation for localized air conditioners in commercial vehicles based on 48 V electrical system. Appl Energy 2018:231.
[4] Jaziri N, Boughamoura A, Muller J, Mezghani B, Tounsi F, Ismail M. A comprehensive review of Thermoelectric Generators: technologies and common applications. Energy Rep 2020;6:264–87.
[5] Li Y, Xiong BY, Vilathgamuwa DM, Wei ZB, Xie CJ, Zou CF. Constrained ensemble kalman filter for distributed electrochemical state estimation of lithium-ion batteries. IEEE T Ind Inform 2021;17:240–50.
[6] Li X, Xie C, Quan S, Shi Y, Tang Z. Optimization of thermoelectric modules' number and distribution pattern in an automotive exhaust thermoelectric generator. IEEE Access 2019;7:72143–57.
[7] Weng CC, Huang MJ. A simulation study of automotive waste heat recovery using a thermoelectric power generator. Int J Therm Sci 2013;71:302–9.
[8] Xiao JS, Yang TQ, Li P, Zhai PC, Zhang QJ. Thermal design and management for performance optimization of solar thermoelectric generator. Appl Energy 2012;93:33–8.
[9] Miljkovic N, Wang EN. Modeling and optimization of hybrid solar thermoelectric systems with thermosyphons. Sol Energy 2011;85:2843–55.
[10] Al-Nimr MA, Tashtoush BM, Khasawneh MA, Al-Keyyam I. A hybrid concentrated solar thermal collector/thermo-electric generation system. Energy 2017;134:1001–12.
[11] Vostrikov S, Somov A, Gotovtsev P. Low temperature gradient thermoelectric generator: modelling and experimental verification. Appl Energy 2019;255.
[12] Sa C, Xu XJ, Wu X, Chen JX, Zuo CL, Fang XS. A wearable helical organic-inorganic photodetector with thermoelectric generators as the power source. J Mater Chem C 2019;7:13097–103.
[13] Ding L, Ruochen W, Wei Y, Zeyu S, Meng Xiangpeng. Modelling and simulation study of a converging thermoelectric generator for engine waste heat recovery. Appl Therm Eng 2019:153.
[14] Gunay O, Abdullah Hakan Y, Rasit A, Kagan Ekrem Calisal. Smart thermoelectric waste heat generator: design, simulation and cost analysis, vol. 37. Sustainable Energy Technologies and Assessments; 2020.
[15] Cao Y, Abu Hamdeh Nidal H, Moria H, Asaadi S, Alsulami R, Sadighi Dizaji Hamed. A novel proposed flexible thin-film solar annular thermoelectric generator. Appl Therm Eng 2021:183.
[16] Evangelos B, Tzivanidis Christos. Energy and financial analysis of a solar driven thermoelectric generator. J Clean Prod 2020:264.
[17] Deng W, Wang XJ, Pan XD, Zhang SX, Ding JJ, Li GP. Geometry design and performance optimization of a terrestrial radioisotope thermoelectric generator based on finite element analysis. Ann Nucl Energy 2021:151.
[18] Poh CS, Chen SW, Wang TY, Chai ML, Lin WK, Wang JR, et al. Analysis of characteristics and performance of thermoelectric modules. In: 5th international symposium on next-generation electronics (isne) 2016; 2016.
[19] Rezania A, Yazawa K, Rosendahl LA, Shakouri A. Co-optimized design of microchannel heat exchangers and thermoelectric generators. Int J Therm Sci 2013;72:73–81.
[20] Rezania A, Rosendahl LA, Yin H. Parametric optimization of thermoelectric elements footprint for maximum power generation. J Power Sources 2014;255:151–6.
[21] Meng JH, Zhang XX, Wang XD. Multi-objective and multi-parameter optimization of a thermoelectric generator module. Energy 2014;71:367–76.
[22] Liu HB, Wang SL, Yang YR, Chen WH, Wang XD. Theoretical analysis of performance of variable cross-section thermoelectric generators: effects of shape factor and thermal boundary conditions. Energy 2020:201.
[23] Sahin AZ, Yilbas BS. The thermoelement as thermoelectric power generator: effect of leg geometry on the efficiency and power generation. Energy Convers Manag 2013;65:26–32.
[24] Yilbas BS, Ali H. Thermoelectric generator performance analysis: influence of pin tapering on the first and second law efficiencies. Energy Convers Manag 2015;100:138–46.
[25] Niu ZQ, Yu SH, Diao H, Li QS, Jiao K, Du Q, et al. Elucidating modeling aspects of thermoelectric generator. Int J Heat Mass Tran 2015;85:12–32.
[26] Shu GQ, Ma XN, Tian H, Yang HQ, Chen TY, Li XY. Configuration optimization of the segmented modules in an exhaust-based thermoelectric generator for engine waste heat recovery. Energy 2018;160:612–24.
[27] Liang XY, Sun XX, Tian H, Shu GQ, Wang YS, Wang X. Comparison and parameter optimization of a two-stage thermoelectric generator using high temperature exhaust of internal combustion engine. Appl Energy 2014;130:190–9.
[28] Fan L, Zhang G, Wang R, Jiao K. A comprehensive and time-efficient model for determination of thermoelectric generator length and cross-section area. Energy Convers Manag 2016:122.
[29] He H, Wu Y, Liu W, Rong M, Fang Z, Tang X. Comprehensive modeling for geometric optimization of a thermoelectric generator module. Energy Conversion and Management; 2019. p. 183.
[30] Lund A, Tian Y, Darabi S, Christian Müller. A polymer-based textile thermoelectric generator for wearable energy harvesting. J Power Sources 2020:480.
[31] Choi Y, Negash A, Kim TY. Waste heat recovery of diesel engine using porous medium-assisted thermoelectric generator equipped with customized thermoelectric modules. Energy Convers Manag 2019:197.
[32] Kaushik SC, Manikandan S. The influence of Thomson effect in the energy and exergy efficiency of an annular thermoelectric generator. Energy Convers Manag 2015;103:200–7.
[33] Shen ZG, Wu SY, Xiao L. Assessment of the performance of annular thermoelectric couples under constant heat flux condition. Energy Convers Manag 2017;150:704–13.
[34] Ge MH, Wang XW, Zhao YL, Wang SX, Liu LS. Performance analysis of vaporizer tube with thermoelectric generator applied to cold energy recovery of liquefied natural gas. Energy Convers Manag 2019;200.
[35] Yang YR, Wang SX, Zhu Y. Evaluation method for assessing heat transfer enhancement effect on performance improvement of thermoelectric generator systems. Appl Energy 2020:263.
[36] Zhang AB, Wang BL, Pang DD, Chen JB, Wang J, Du JK. Influence of leg geometry configuration and contact resistance on the performance of annular thermoelectric generators. Energy Convers Manag 2018;166:337–42.
[37] Shen Z-G, Wu S-Y, Xiao L. Assessment of the performance of annular thermoelectric couples under constant heat flux condition. Energy Convers Manag 2017;150:704–13.
[38] Liu H-B, Wang S-L, Yang Y-R, Chen W-H, Wang X-D. Theoretical analysis of performance of variable cross-section thermoelectric generators: effects of shape factor and thermal boundary conditions. Energy 2020:201.
[39] Haoqi Y, Gequn S, Hua T, Xiaonan M, Tianyu C, Liu Peng. Optimization of thermoelectric generator (TEG) integrated with three-way catalytic converter (TWC) for harvesting engine's exhaust waste heat. Appl Therm Eng 2018:144.
[40] Dirk E, Martin J, Markus B, Alexandre J, Böttner Harald. Multiphysics simulation of thermoelectric systems for comparison with experimental device performance. J Electron Mater 2009;38.
[41] Fuqiang C, Yanji H, Wenli Z, Zhu Chao. Performance prediction and test of a Bi 2 Te 3 -based thermoelectric module for waste heat recovery. J Therm Anal

Calorim 2014:118.
[42] Shen Z-G, Wu S-Y, Xiao L, Yin G. Theoretical modeling of thermoelectric generator with particular emphasis on the effect of side surface heat transfer. Energy 2016;95:367–79.
[43] Amin N, Francisco S, Dycus JH, Matthew JC, James ML, Mehmet CÖ, et al. Thermoelectric generators for wearable body heat harvesting: material and device concurrent optimization. Nanomater Energy 2020:67.
[44] Muthu G, Shanmugam S, Veerappan AR. Theoretical and experimental study on a thermoelectric generator using concentrated solar thermal energy. J Electron Mater 2019;48.
[45] Tan Q, Chen G, Sun Y, Duan B, Li G, Zhai P. Performance of annular thermoelectric couples by simultaneously considering interface layers and boundary conditions. Appl Therm Eng 2020:174.
[46] Shen Z-G, Wu S-Y, Xiao L. Theoretical analysis on the performance of annular thermoelectric couple. Energy Convers Manag 2015;89:244–50.
[47] Chen G. Theoretical efficiency of solar thermoelectric energy generators. J Appl Phys 2011;109.
[48] Yazawa K, Shakouri A. Optimization of power and efficiency of thermoelectric devices with asymmetric thermal contacts. J Appl Phys 2012;111.